Modeling of all-porous solid oxide fuel cells with a focus on the optimization of electrolyte porosity

Haoran Xu[1,2], Bin Chen[1], Peng Tan[1], Jin Xuan[2], M. Mercedes Maroto-Valer[2*], David Farrusseng[3], Qiong Sun[4], Meng Ni[1,5*]

[1] Building Energy Research Group, Department of Building and Real Estate The Hong Kong Polytechnic University, Hung Hom, Kowloon, Hong Kong, China

[2] Research Centre for Carbon Solutions (RCCS), School of Engineering & Physical Sciences, Heriot-Watt University, Edinburgh, EH14 4AS, United Kingdom

[3]Institut de Recherches sur la Catalyse et l'Environnement de Lyon, IRCELYON, Université Lyon 1, CNRS. 2, Av. Albert Einstein F-69626, Villeurbanne, France

[4] School of Civil and Transportation Engineering, Guangdong University of Technology, Guangzhou 510006, China

[5] Environmental Energy Research Group, Research Institute for Sustainable Urban Development (RISUD), The Hong Kong Polytechnic University, Hung Hom, Kowloon, Hong Kong, China

Abstract:

Conventional solid oxide fuel cells (SOFCs) could suffer from carbon deposition when fueled with hydrocarbons. For comparison, a new type of SOFC with porous electrolyte can resist carbon deposition because it allows oxygen molecules to transport from the cathode to the anode. As the transport of O_2 to the anode lowers the fuel cell performance and causes the risk of explosion, the rate of O_2 transport must be well controlled to ensure efficient and safe operation. Following our previous model, this paper focuses on electrolyte porosity optimization under various inlet methane mole fractions, inlet oxygen mole fractions and inlet

gas flow rates. Furthermore, a new design with a partial porous electrolyte is proposed and numerically evaluated. The new design significantly improves the electrochemical performance compared with all-porous one. A conversion rate > 90% from methane to syngas is achieved at the 0.33 inlet CH_4 mole fraction with the new design. The results enhance the understanding of all porous solid oxide fuel cells and the mechanism underlying, inspiring novel designs of solid oxide fuel cells.

Keywords: All porous solid oxide fuel cell; Methane coking; Carbon deposition; Mathematical modeling; novel design

---

* Corresponding authors:

Email: M.Maroto-Valer@hw.ac.uk; Tel: +44 (0) 131 451 8028;

Email: bsmengni@polyu.edu.hk; Tel: 852-27664152; Fax: 852-27645131 (NI M).

1. Introduction

Solid oxide fuel cells (SOFCs) are highly efficient and clean power generation devices. An SOFC has a whole solid structure, where dense electrolyte is sandwiched between porous anode and cathode [1-3]. The high operating temperature (about 800 ^{o}C) not only favors the combined heat and power cogeneration systems [4, 5], but also allows non-noble metal (such as nickel) to be used as catalyst and various fuels (H_2, CO, C_nH_m, NH_3) can be utilized [6-8]. Methane is an attractive fuel choice for SOFCs due to its low price and high volumetric energy density compared with H_2 and CO [9-11]. However, methane coking and carbon deposition in the anode is a severe problem especially when nickel is used [12-14]. Apart from using novel anode materials, Guo et al. proposed a new structure, all porous SOFC (AP-SOFC) [15, 16], an SOFC with a porous electrolyte to resist carbon deposition. In the AP-SOFC, O_2 molecules can move from the cathode to anode and react with methane and deposited carbon (if any) directly, inhibiting its coking and carbon deposition on anode. A 2000-hour stable operation was achieved in the preliminary experimental test using CH_4 fuel without any external reformer or steam addition. Moreover, no carbon deposition was detected on anode after test. In addition to the experimental demonstration of this novel concept, numerical simulations were conducted to better understand the detailed mechanism of AP-SOFCs in carbon deposition resistance and their potential for further electrochemical performance improvement [17]. Through the models, the determining role of oxygen diffusion in improving oxygen-to-carbon ratio on anode surface was demonstrated. An electrochemical performance improvement was also obtained by altering the mole fraction of inlet species and adopting anode-supported SOFC in the model.

No doubt, the key to achieve a good balance among electrochemical performance, carbon resistance and safety heavily relies on the O_2 gas transport process through the porous electrolyte, which depends on the porous structure properties of the electrolyte. However, the detailed analyses on the electrolyte porous structure properties have not been conducted yet. The electrolyte porosity is an important factor, which affects gas diffusion between electrodes, electrolyte ionic conductivities, and thus determines the cell performance.

To fill this research gap, numerical studies have been conducted in this work to investigate the effects of electrolyte porosity on the cell performance. Moreover, a novel design of tubular cell is proposed for the first time to achieve improved electrochemical performance and safe operation simultaneously. In addition, in this paper the tubular cell models are extended from the original button cell model and validated by experimental data.

2. Model description

A 2D mathematical model for button AP-SOFC is developed and validated by experimental data. The model is further extended to tubular AP-SOFCs for parametric studies for practical application. In the models, electrochemical/chemical reactions, ion/electron conduction and mass/momentum transportation are fully considered. The schematics of both button AP-SOFC and tubular AP-SOFC are shown in Fig.1(a) and Fig. 1(b), respectively. In consistence with the experimental work conducted by Guo et al., the AP-SOFCs in this study adopt porous $Gd_{0.1}Ce_{0.9}O_{1.9}$ (CGO) electrolyte as support layer with a thickness of 2 mm. The thickness of Ni-CGO anode and $Ba_{0.5}Sr_{0.5}Co_{0.8}Fe_{0.2}O_{3-\delta}$ (BSCF) cathode are 55 μm and 25 μm,

respectively. The surface area of button AP-SOFC is 2.54 cm^2 and the length of tubular AP-SOFC is 1.8 cm. Related material properties, kinetic parameters and other tuning parameters can be found in Table 1 and Table 2.

In the operation of tubular AP-SOFCs, CH_4 and O_2 are introduced into anode and cathode channels, respectively. Apart from flowing along the cell length to the outlet, O_2 and CH_4 can also diffuse through the porous electrolyte and react with each other. The reaction between O_2 and CH_4 generates CO_2 and H_2O, and the generated H_2O can further react with CH_4 (methane steam reforming, MSR) to produce H_2 and CO. Both H_2 and CO can electrochemically react with O^{2-} ions and release electrons for power generation. H_2O generated from the electrochemical reactions will further react with CH_4 and the reaction chain among H_2O, CH_4 and O^{2-} continues if there is enough CH_4 and O_2. H_2 and CO will also react with O_2 to form H_2O and CO_2, respectively. Due to the existence of H_2O and CO, water gas shift reaction (WGSR) catalyzed by nickel is also considered in the anode.

2.1 Model assumptions

In accordance with previous model on SOFCs, assumptions (1~5) are adopted. For the study of electrolyte porosity change in AP-SOFCs, assumption (6) is used to define its ionic conductivity.

(1) The area of triple phase boundary (TPB) shared by H_2 and CO for electrochemical reaction is proportional to their local mole fraction.

(2) Electrochemical reaction sites are distributed uniformly in the whole porous electrode.

(3) Both ionic- and electronic- conducting phases in the porous electrodes are homogeneous and continuous.

(4) Gases in the model follow ideal gas law.

(5) Temperature distribution is uniform in the cell due to its small size.

(6) Ionic conductivity of porous CGO is inversely proportional to its porosity in the porosity range, 0.3 to 0.7.

(7) The electronic conductivity of the CGO electrolyte is not considered.

2.2 Chemical reactions

The porous electrolyte allows the diffusion of gases between the anode and the cathode, hence enabling chemical oxidization of CH_4 (R_{MO}) as shown in Eq. (1).

$$CH_4 + 2O_2 = CO_2 + 2H_2O \qquad (1)$$

It should be noted that the methane oxidation rate in anode is much higher than that in other areas due to the catalytic effects of nickel. The effects of active surface area for the chemical reactions are also included in the pre-exponential factor, which is tuned to fit the experimental data in the model validation part. H_2O generated by methane oxidization can further react with CH_4 through MSR reaction, as shown in Eq. (2).

$$CH_4 + H_2O \leftrightarrow CO + 3H_2 \qquad (2)$$

MSR is the key reaction in AP-SOFCs as it provides suitable fuel (H_2 and CO) for electrochemical reactions.

Chemical oxidizations of H_2 (R_{HO})

$H_2 + 0.5O_2 = H_2O$ (3)

and chemical oxidization of CO (R_{CO})

$CO + 0.5O_2 = CO_2$ (4)

also exist in the cell. However, these two reactions are not preferred in AP-SOFCs as they not only reduce the electrochemical performance but also bring in the risk of explosion.

Water gas shift reaction (R_{WGSR}) catalyzed by nickel in the porous anode is considered and can be described as Eq. (5) below:

$CO + H_2O \leftrightarrow CO_2 + H_2.$ (5)

2.3 Electrochemical reaction

In the cathode, O_2 molecules are reduced to O^{2-}, as shown in Eq. (6).

$O_2 + 4e^- = 2O^{2-}$ (6)

The generated O^{2-} ions can transport through electrolyte to anode, where they electrochemically react with H_2 and CO and release electrons for power generation as shown in Eq. (7) and Eq. (8).

$H_2 + O^{2-} = H_2O + 2e^-$ (7)

$CO + O^{2-} = CO_2 + 2e^-$ (8)

The overall electrochemical reactions of H_2 and CO as fuel and O_2 as oxidant can be written as Eq. (9) and Eq. (10).

$H_2 + 0.5O_2 = H_2O$ (9)

$CO + 0.5O_2 = CO_2$ (10)

Equilibrium potentials (E_{H_2} and E_{CO}) for Eq. (9) and Eq. (10) are calculated as follows:

$$E_{H_2} = E^0_{H_2} + \frac{RT}{2F}\ln\left[\frac{P^L_{H_2}(P^L_{O_2})^{1/2}}{P^L_{H_2O}}\right] \qquad (11)$$

and

$$E_{CO} = E^0_{CO} + \frac{RT}{2F}\ln\left[\frac{P^L_{CO}(P^L_{O_2})^{1/2}}{P^L_{CO_2}}\right], \qquad (12)$$

where $E^0_{H_2}$ and E^0_{CO} are the respective standard potentials, R is the universal gas constant, T is the operating temperature and F is the Faraday constant. $P^L_{H_2}$, $P^L_{H_2O}$, P^L_{CO} and $P^L_{CO_2}$ are the anode local gas partial pressures for H_2, H_2O, CO and CO_2, respectively. $P^L_{O_2}$ is the cathode local O_2 partial pressure. The values of E^0_{CO} and $E^0_{H_2}$ can be calculated by Eq. (13) and Eq. (14).

$$E^0_{H_2} = 1.253 - 0.00024516T \text{ (V)} \qquad (13)$$

$$E^0_{CO} = 1.46713 - 0.0004527T \text{ (V)} \qquad (14)$$

For the calculation of cell's equilibrium potential, a parallel scheme is used as suggested in ref. [18]. Considering the different overpotential losses involved in electrochemical oxidation of H_2 and CO, the operating potential can be calculated by deducting overpotential losses from equilibrium potential [19, 20]

$$V = E_{eq} - \eta_{act} - \eta_{ohmic}, \qquad (15)$$

where η_{act} is the activation overpotential loss and η_{ohmic} is the ohmic overpotential loss. η_{act} stems from the activation barrier of the electrochemical reactions, which is strongly related with the reactions occurred and the electrode property. η_{act} can be described by Butler-Volmer equation

$$i = i_0\left\{\exp\left(\frac{\alpha nF\eta_{act}}{RT}\right) - \exp\left(-\frac{(1-\alpha)nF\eta_{act}}{RT}\right)\right\}, \qquad (16)$$

where i is the operating current density, α is the electron transfer coefficient and n is the number of transferred electrons per electrochemical reaction. The exchange current density (i_0) can be expressed as

$$i_0 = \gamma \exp\left(-\frac{E_{act}}{RT}\right), \qquad (17)$$

where γ is the pre-exponential factor and E_{act} is the activation energy. The pre-exponential factor γ for H_2 electrochemical oxidation is set to be 2.2 times of the γ for CO electrochemical oxidation, while their activation energy is set to be the same as suggested by Luo et al. [21].

η_{ohmic} is caused by ionic/electronic resistance in the cell and can be calculated by Ohm law. It should be noted that the mass-transport-related overpotential loss is already considered by using local gas partial pressure for equilibrium potential calculation in Eq. (11) and Eq. (12). Parameters for above electrochemical reactions can be found in Table 3.

2.4 Mass and momentum transport

Mass transport of gas species is governed by Eq. (18)[22] as

$$N_j = -\frac{1}{RT}\left(\frac{B_0 y_j P}{\mu}\nabla P - D_j^{eff}\nabla(y_j P)\right) \ (j = 1, \dots, n), \qquad (18)$$

where B_0 is the permeability, μ is the gas viscosity, y_j is the mole fraction component j and D_j^{eff} is the overall effective diffusion coefficient. D_j^{eff} is determined by

$$D_j^{eff} = \frac{\varepsilon}{\tau}\left(\frac{1}{D_{jm}^{eff}} + \frac{1}{D_{jk}^{eff}}\right)^{-1}, \qquad (19)$$

where ε is the porosity, τ is the tortuosity factor, D_{jm}^{eff} is molecular diffusion coefficient and D_{jk}^{eff} is Knudsen diffusion coefficient [23, 24].

The mass conservation can be described by

$$\nabla\left(-D_j^{eff}\nabla c_j\right) = R_j, \qquad (20)$$

where c_j is the gas molar concentration and R_j is the mass source term of the gaseous species.

Momentum transport is governed by Navier-Stokes equation with Darcy's term as

$$\rho\frac{\partial u}{\partial t} + \rho u\nabla u = -\nabla p + \nabla\left[\mu\left(\nabla u + (\nabla u)^T\right) - \frac{2}{3}\mu\nabla u\right] - \frac{\varepsilon\mu u}{k}, \qquad (21)$$

where ρ is the gas density, u is the velocity vector and k is the permeability of the porous material.

2.5 Boundary conditions and model solution

At the outside surface of the two electrodes, electric ground and applied voltage are specified on anode and cathode, respectively. At the channel inlets, gas flow rate and species molar fractions are given. At the channel outlets, pressure condition is specified. At the ends of the cell, zero flux is specified.

The model is built at given operating parameters such as temperature, voltage, and inlet gas flow rate and species mole fraction. The governing equations are solved through finite element analysis in the commercial software COMSOL MULTIPHYSICS®.

3 Results and discussion

3.1 Model validation and criteria for safe operation

In accordance with the experiments, the button AP-SOFC model employs the same material properties and the same structural parameters as in ref.[15]. The button cell model is validated

by comparing the simulated I-V curves with experimental data, as shown in Fig. 1(c) with high accuracy. For model development, the tuning parameters are restricted in the pre-exponential factors for chemical/electrochemical oxidations. The other parameters adopted are from experimental tests and literatures. Therefore, the model is validated and suitable for subsequent parametric study. The same material properties and tuning parameters are used when the button cell is extended to a tubular AP-SOFC for the study of practical operation. The I-V-P characteristics comparison between a button AP-SOFC and a tubular AP-SOFC is shown in Fig. 1(d). The small difference indicates the extensibility of the model.

Although the long-term operation of AP-SOFCs has already been proved experimentally, the rather dilute inlet gas (CH_4 4% as fuel and O_2 4% as oxidant) is not suitable for practical operation. Therefore, the mole fraction of O_2 and CH_4 is raised to a higher level in the following parametric studies. In addition, safe operation criteria are set considering possible carbon deposition and explosion risk.

To evaluate the possibility of methane coking, oxygen-to-carbon ratio (O/C ratio) larger than 1.5 on anode surface is adopted as the criterion according to fuel cell handbook[25]. O refers to the total oxygen atoms from steam and air, i.e., one mole O_2 and H_2O provide two moles and one mole oxygen atoms, respectively. C refers to carbon atoms from CH_4, i.e., one mole CH_4 provides one mole carbon atoms. It should be noted that only O_2 and H_2O are considered as oxygen atom supplier because they are the main oxidants in the anode and have a fast reaction rate with methane.

To evaluate the risk of explosion, the concentrations of CH_4, H_2 and CO are suggested to be

smaller than the “Lower Explosive Limit”, which are 5%, 4% and 12% in air (oxygen), respectively. Therefore, mole fraction product of $CH_4 \times O_2$ equal to 1.05%, $H_2 \times O_2$ equal to 0.84% and $CO \times O_2$ equal to 2.52% are regarded as the maximum products in this paper for the safe operation of AP-SOFCs. It should be noted that the above limitation values are adopted at room temperature and the explosive range expands with increasing temperature. Here, the focus of the paper is to enhance the performance of AP-SOFC by controlling the cell microstructure. To ensure safety of the AP-SOFC, the operating conditions must be more carefully controlled.

3.2 Effects of electrolyte porosity

In the electrolyte-supported AP-SOFC, the electrolyte porosity plays an important role in determining the cell performance. Generally, O_2 diffusion from cathode to anode becomes easier at high electrolyte porosity, which helps to improve O/C ratio and inhibits methane coking in the anode. However, a higher porosity results in lower open circuit voltage (OCV) and smaller ionic conductivity, which largely increases the ohmic potential loss and decreases electrochemical performance of the AP-SOFC. For the parametric study in this section, the electrolyte porosity is altered between 0.3 and 0.7. Air is used as cathode inlet gas and 0.35 mole fraction of CH_4 is used as anode inlet gas. The applied voltage, operating temperature and inlet flow rate are 0.5 V, 923 K and 100 SCCM, respectively.

With the electrolyte porosity increasing from 0.3 to 0.7, the O_2 diffusion from cathode to anode becomes easier, as a result, the average O/C ratio at anode surface increases from 0.9 to 1.6 as

shown in Fig. 2(a). Nevertheless, the current density decreases from 43 mA cm^{-2} to 16 mA cm^{-2} due to the low electrolyte ionic conductivity and reduced open circuit voltage (OCV) at high electrolyte porosity.

The distribution of $CH_4 \times O_2$ mole fraction product is shown in Fig. 2(b) to investigate the potential of fuel explosion. For both 0.3 and 0.7 electrolyte-porosity cases, the peak value of $CH_4 \times O_2$ product is in the middle of electrolyte close to inlet, where CH_4 and O_2 are well mixed before heavily consumed. The peak value of the product (1.3×10^{-2}) in the 0.3 electrolyte-porosity case is higher than the criteria (1.05×10^{-2}), indication the risk of explosion in the inlet area. Whereas in the 0.7 electrolyte-porosity case, the peak value of the product (1.02×10^{-2}) is lower than the criteria as more CH_4 and O_2 are consumed due to better diffusion at high porosity.

The distributions of H_2 and CO at different electrolyte-porosity cases are also as shown in Fig. 2(c). The high mole fraction of outlet syngas (0.23 at 0.3 electrolyte-porosity case) compared with the inlet methane (0.35) indicates the potential for syngas and power co-generation in AP-SOFCs [26]. However, the H_2 and CO are severely consumed at 0.7 electrolyte-porosity case due to the easier transport for gas molecules between anode and cathode, where the conversion ratio from methane to syngas is declined to less than 0.4.

3.3 Effect of anode inlet CH_4 mole fraction

CH_4, as the fuel source for power generation in the AP-SOFC, is also the cause of carbon deposition and explosion. The mole fraction of CH_4 is diluted to 4% in the experiments for safe

operation, while such a low mole fraction is not suitable for practical applications. For the parametric studies in this section, air is used as cathode inlet gas and anode inlet CH_4 mole fraction is altered in the range between 0.04 and 1 to investigate its effect on cell performance. The applied voltage, operating temperature and inlet flow rate are 0.5 V, 923 K and 100 SCCM, respectively. The cell performance under 0.3, 0.5 and 0.7 electrolyte porosities are compared.

The increase of inlet CH_4 mole fraction shows significant enhancement on AP-SOFC's electrochemical performance (Fig. 3(a)) and syngas generation (Fig. 3(b)). The current density is improved from 22 mA cm^{-2} to 48 mA cm^{-2} when the inlet CH_4 mole fraction is increased from 0.04 to 1. Regarding the effect of electrolyte porosity, the current density is increased more significantly at an electrolyte porosity of 0.3, in comparison with electrolyte porosity of 0.5 and 0.7. Apart from high current density, the syngas generation is also very good at 0.3 electrolyte porosity. When the inlet CH_4 mole fraction reaches 0.5, the methane utilization rate achieves 74%, together with a 61% conversion rate from methane to syngas. Nevertheless, the methane utilization rate is quite low at high inlet CH_4 mole fraction.

A high inlet CH_4 mole fraction is also not suggested for practical operation considering methane coking and fuel explosion. Fig. 3(c) shows the anode surface O/C ratio change along with the increasing inlet CH_4 mole fraction in different electrolyte-porosity cases. The O/C ratio is very sensitive to the change of inlet CH_4 mole fraction. With the increase of inlet CH_4 mole fraction, the O/C ratio declines quickly. To meet the criterion of O/C ratio > 1.5, only an inlet CH_4 mole fraction < 0.31 is allowed at an electrolyte porosity of 0.3 and the inlet CH_4 mole fraction limitation can be raised to 0.35 at an electrolyte porosity of 0.7. As shown in Fig.

3(d), the limitation of inlet CH_4 mole fraction can be raised at higher electrolyte porosity in the restriction of fuel explosion criterion.

3.4 Effect of inlet gas flow rate

The inlet gas flow rate is related to the size of SOFC. A small flow rate usually causes a high fuel utilization ratio while undermines the electrochemical performance. For parametric studies in this section inlet gas flow rate is altered in the range between 1 SCCM to 100 SCCM. The operating temperature is 923 K at an applied voltage of 0.5 V. Pure O_2 and pure CH_4 are used as cathode and anode inlet gas, respectively. The cell performance under 0.3, 0.5 and 0.7 electrolyte porosities are compared.

As shown in Fig.4, by decreasing both anode and cathode inlet gas flow rate from 100 SCCM to 1 SCCM, a smaller current density (Fig. 4(a)) and higher CH_4 utilization rate (Fig. 4(b)) are observed, whereas a high inlet gas flow rate results in a high outlet syngas mole fraction (0.38 for H_2 and 0.17 for CO at 100 SCCM).

Moreover, the inlet gas flow rate has great effect on anode surface O/C ratio as shown in Fig. 4(c). With the decrease of inlet gas flow rate from 100 SCCM to 40 SCCM, the average O/C ratio on anode surface increases from 1 to 20, because H_2O generation rate from electrochemical reaction becomes relatively higher compared with the decreased inlet methane rate. Such a huge increase indicates that decreasing inlet gas flow rate to a suitable level is an easy and effective method to inhibit methane coking. The O/C ratio distribution along cell length is also given in Fig. 4(d). The O/C ratios contributed by H_2O and O_2 are both growing

along the cell length, mainly due to the continual consumption of CH_4. Meanwhile, H_2O contributes more oxygen atoms compared with O_2 and the difference becomes larger along the cell because H_2O molecules are continually generated by electrochemical oxidization of H_2 while no O_2 is generated.

3.5 Design of partial porous electrolyte

From the above analyses, several conclusions can be reached for optimization of AP-SOFC design and performance. Firstly, there is less possibility for fuel explosion at higher porosity (a porosity of 0.7 is safer than 0.3 as shown in section 3.2). Secondly, a higher inlet methane mole fraction offers better electrochemical performance while lowers the O/C ratio (22 mA cm^{-2} at 0.04 inlet methane mole fraction vs 48 mA cm^{-2} using pure methane as shown in section 3.3). However, the possibilities for methane coking and fuel explosion are also raised with the increase of inlet methane mole fraction. Thirdly, a lower inlet gas flow rate is helpful in inhibiting methane coking (the average O/C ratio on anode surface increasing from 1 to 20 with the inlet gas flow rate decreasing from 100 SCCM to 40 SCCM as shown in section 3.4). Lastly, a low electrolyte porosity benefits electrochemical performance improvement of an electrolyte supported AP-SOFC (43 mA cm^{-2} at 0.3 porosity vs to 16 mA cm^{-2} at 0.7 porosity as shown in section 3.1) and the O/C ratio becomes higher along the cell length (as shown in Fig. 4(d)). Therefore, an AP-SOFC with high electrochemical performance can be safely operated with suitable operating parameters, as discussed below. Furthermore, the dense electrolyte can be adopted in the area away from inlet, where steam to oxygen ratio is high enough to prevent

methane coking.

Based on these conclusions, an SOFC with a partial porous electrolyte is proposed and evaluated in this section. In this new design, first half (9 mm) of the electrolyte has a porosity of 0.42 (the same with ref. [15]), while the other half of the electrolyte is dense. Air is used as cathode inlet gas and 0.33 mole fraction of CH_4 is used as anode inlet gas. The applied voltage, operating temperature and inlet flow rate are 0.5 V, 923 K and 6 SCCM, respectively.

Compared with the AP-SOFC, the SOFC with partial porous electrolyte shows a much higher electrochemical performance as shown in Fig. 5(a). By decreasing the ohmic loss, the peak power density raises from 13.6 mW cm^{-2} to 31.6 mW cm^{-2}, showing a 130% improvement. The SOFC with partial porous electrolyte also shows a high O/C ratio (Fig. 5(b)), which decreases with the increase of applied voltage and keeps larger than 30 at 1 V. Moreover, low $CH_4 \times O_2$ value (Fig. 5(c)) is also obtained in the newly designed SOFC, where the mole fraction product of $CH_4 \times O_2$ keeps lower than the risk value even at 1.0 V applied voltage. By meeting both these two criteria, the SOFC with partial porous electrolyte is very promising for long-term safe operation. In addition, this newly designed SOFC shows a high methane conversion rate (~ 0 methane mole fraction in the outlet) and the generation of syngas as byproduct Fig. 5(d) also shows its potential for better economic advantages.

3.6 Possible applications of AP-SOFCs

The present study demonstrated that the performance of AP-SOFC could be improved by proper control of the cell microstructure and operating conditions. As demonstrated in Ref. [17], the peak power density can reach 0.16 $W.m^{-2}$ for an anode-supported AP-SOFC. In that

simulation, the electrolyte microstructure and operating conditions were not optimized. It is expected that the performance of anode-supported AP-SOFC could be further improved by adjusting the electrolyte porosity, pore size, the pressure at the two electrodes, etc. With improved performance, the AP-SOFC could be applied as a power source using various hydrocarbon fuels, such as natural gas, biogas, or ethanol. However, if the SOFC system is designed for operation on H_2, the AP-SOFC concept is not suggested since there is no carbon deposition risk and the transport of gases through the porous electrolyte only reduces the cell performance.

4 Conclusions

Mathematical models of all-porous solid oxide fuel cells are developed with various parametric studies in this paper. From the parametric study of electrolyte porosity change, it is found that a high electrolyte porosity helps raise oxygen-to-carbon (O/C) ratio and lower $CH_4 \times O_2$ mole fraction product due to better gas diffusion. Nevertheless, a high porosity results in low ionic conductivity of electrolyte, which significantly increases ohmic loss and decreases the electrochemical performance of the cell.

Besides, an SOFC with partial porous electrolyte is proposed. At selected operating parameters, the novel designed SOFC displays a 1.3 times higher electrochemical performance compared with the old design. The high O/C ratio and low $CH_4 \times O_2$ mole fraction product also ensures a long-term safe operation of the cell. Therefore, this design is very promising to safely utilize methane for power generation with syngas as byproduct.

It should be noted that only electrolyte-supported type is analyzed in this paper, considering the much smaller ohmic overpotential in anode-supported solid oxide fuel cells, further improvement is possible for practical application by controlling the operating conditions and proper electrode/electrolyte design. With good cell performance and good carbon resistance, the AP-SOFC could be promising for practical applications. In addition, a detailed analysis on the thermal effects in the all-porous solid oxide fuel cell is needed to consider the different breakdown of heat source compared with traditional methane-fed solid oxide fuel cells. The related effects brought by the thermal effect will also be of interest for its practical application.

Acknowledgements

This research is supported by a grant (F-PolyU501/15) from Research Grant Council (France/HK Joint Research Scheme), University Grants Committee, Hong Kong SAR, a grant from Environment and Conservation Fund (ECF 54/2015), Hong Kong SAR, and a grant from Research Institute for Sustainable Urban Development (RISUD) (1-ZVEA), as well as financial support provided by the Engineering and Physical Sciences Research Council (EP/K021796/1), EPSRC (EP/N009924/1) and the Research Centre for Carbon Solutions (RCCS) at Heriot–Watt University.

Nomenclature

Abbreviation

AP-SOFC	All porous solid oxide fuel cell

BSCF	Barium strontium cobalt ferrite ($Ba_{0.5}Sr_{0.5}Co_{0.8}Fe_{0.2}O_{3-\delta}$)
CGO	gadolinium-doped ceria ($Gd_{0.1}Ce_{0.9}O_{1.9}$)
CMO	Carbon monoxide oxidization
HO	Hydrogen oxidization
MO	Methane oxidization
MSR	Methane steam reforming
O/C	Oxygen to carbon
SCCM	Standard cubic centime per minute
SOFC	Solid oxide fuel cell
WGS	Water gas shift

Roman

B_0	Permeability coefficient, m^2
c_{CO_2}	Mole concentration of carbon dioxide, $mol \cdot m^{-3}$
c_{H_2O}	Mole concentration of water, $mol \cdot m^{-3}$
D_i^{eff}	Effective diffusivity of species i, $m^2 \cdot s^{-1}$
D_{ik}^{eff}	Knudsen diffusion coefficient of i, $m^2 \cdot s^{-1}$
D_{im}^{eff}	Molecular diffusion coefficient of i, $m^2 \cdot s^{-1}$
E_{act}	Activation energy, $J \cdot mol^{-1}$
E_{CO}	Equilibrium potential for carbon monoxide oxidization, V
E_{CO}^0	Standard equilibrium potential for carbon monoxide oxidization, V

E_{eq}	Equilibrium Nernst potential, V
E_{H_2}	Equilibrium potential for hydrogen oxidization, V
$E_{H_2}^0$	Standard equilibrium potential for hydrogen oxidization, V
F	Faraday constant, 96485 C·mol^{-1}
i	Operating current density, A·m^{-2}
i_o	Exchange current density, A·m^{-2}
n	Number of electrons transferred per electrochemical reaction
N_i	Flux of mass transport, kg·m^{-3}·s^{-1}
p	(partial) Pressure, Pa
P_{CO}^L	Local CO partial pressures, Pa
$P_{CO_2}^L$	Local CO_2 partial pressures, Pa
$P_{H_2}^L$	Local H_2 partial pressures, Pa
$P_{H_2O}^L$	Local H_2O partial pressures, Pa
$P_{O_2}^L$	Local O_2 partial pressures, Pa
R	Gas constant, 8.314 J·mol^{-1}·K^{-1}
R_{CMO}	Carbon monoxide oxidization reaction
R_{HO}	Hydrogen oxidization reaction
R_{MSR}	Methane steam reforming reaction
R_{MO}	Methane oxidization reaction
R_{WGS}	Water gas shift reaction
T	Temperature, K

u	Velocity field, $m^3 \cdot s^{-1}$
V	Volume fraction
y_i	Mole fraction of component i

Greek letters

α	Charge transfer coefficient
ε	Porosity
η_{act}	Activation overpotential loss, V
η_{ohmic}	Ohmic overpotential loss, V
κ	Permeability, m^2
μ	Dynamic viscosity of fluid, Pa·s
ρ	Fluid density, $kg \cdot m^{-3}$
σ	Conductivity, S/m
γ	Pre-exponential factor, $A\ m^{-2}$
τ	Tortuosity

Subscripts

an	Anode
ca	Cathode
CH_4	Methane
CO	Carbon monoxide

CO_2	Carbon dioxide
el	Electrolyte
H_2	Hydrogen
l	Ionic phase
O_2	Oxygen
s	Electronic phase

Superscripts

0	Parameter at equilibrium conditions
eff	Effective
L	Local

Reference

[1] Singhal SC. Advances in solid oxide fuel cell technology. Solid State Ionics. 2000;135:305-13.

[2] Ormerod RM. Solid oxide fuel cells. Chemical Society Reviews. 2003;32:17-28.

[3] Cai WZ, Liu J, Yu FY, Zhou Q, Zhang YP, Wang XQ, Liu ML, Ni M, A high performance direct carbon solid oxide fuel cell fueled by Ca-loaded activated carbon, International Journal of Hydrogen Energy. 2017. 42(33):21167-21176.

[4] Xu H, Chen B, Tan P, Zhang H, Yuan J, Liu J, Ni M. Performance improvement of a direct carbon solid oxide fuel cell system by combining with a Stirling cycle. Energy. 2017. 140 (part 1): 979-987.

[5] Zhang HC, Chen B, Xu HR, Ni M. Thermodynamic assessment of an integrated molten carbonate fuel cell and absorption refrigerator hybrid system for combined power and cooling applications. International Journal of Refrigeration. 2016. 70: 1-12.

[6] Minh NQ. Solid oxide fuel cell technology—features and applications. Solid State Ionics. 2004;174:271-7.

[7] Sharma M, N R, Dasappa S. Solid oxide fuel cell operating with biomass derived producer gas: Status and challenges. Renewable and Sustainable Energy Reviews. 2016;60:450-63.

[8] Ni M. Thermo-electrochemical modeling of ammonia-fueled solid oxide fuel cells considering ammonia thermal decomposition in the anode. International Journal of Hydrogen

Energy. 2011;36:3153-66.
[9] Kee RJ, Zhu H, Goodwin DG. Solid-oxide fuel cells with hydrocarbon fuels. Proceedings of the Combustion Institute. 2005;30:2379-404.
[10] Gür TM. Comprehensive review of methane conversion in solid oxide fuel cells: Prospects for efficient electricity generation from natural gas. Progress in Energy and Combustion Science. 2016;54:1-64.
[11] Buonomano A, Calise F, d'Accadia MD, Palombo A, Vicidomini M. Hybrid solid oxide fuel cells–gas turbine systems for combined heat and power: A review. Applied Energy. 2015;156:32-85.
[12] Pillai M, Lin Y, Zhu H, Kee RJ, Barnett SA. Stability and coking of direct-methane solid oxide fuel cells: Effect of CO2 and air additions. Journal of Power Sources. 2010;195:271-9.
[13] Yan M, Zeng M, Chen Q, Wang Q. Numerical study on carbon deposition of SOFC with unsteady state variation of porosity. Applied Energy. 2012;97:754-62.
[14] Xiao J, Xie Y, Liu J, Liu M. Deactivation of nickel-based anode in solid oxide fuel cells operated on carbon-containing fuels. Journal of Power Sources. 2014;268:508-16.
[15] Guo Y, Bessaa M, Aguado S, Steil MC, Rembelski D, Rieu M, et al. An all porous solid oxide fuel cell (SOFC): a bridging technology between dual and single chamber SOFCs. Energy & Environmental Science. 2013;6:2119-23.
[16] Guo YM, Largiller G, Guizard C, Tardivat C, Farrusseng D. Coke-free operation of an all porous solid oxide fuel cell (AP-SOFC) used as an O2 supply device. Journal of Materials Chemistry A. 2015;3:2684-9.
[17] Xu H, Chen B, Tan P, Cai W, He W, Farrusseng D, et al. Modeling of all porous solid oxide fuel cells. Applied Energy. 2018;219:105-13.
[18] Ni M, Modeling of SOFC running on partially pre-reformed gas mixture, International Journal of Hydrogen Energy. 2012; 37(2): 1731-1745.
[19] Xu H, Chen B, Liu J, Ni M. Modeling of direct carbon solid oxide fuel cell for CO and electricity cogeneration. Applied Energy. 2016;178:353-62.
[20] Xu H, Chen B, Ni M. Modeling of Direct Carbon-Assisted Solid Oxide Electrolysis Cell (SOEC) for Syngas Production at Two Different Electrodes. J Electrochem Soc. 2016;163:F3029-F35.
[21] Luo Y, Shi Y, Li W, Cai N. Comprehensive modeling of tubular solid oxide electrolysis cell for co-electrolysis of steam and carbon dioxide. Energy. 2014;70:420-34.
[22] Suwanwarangkul R, Croiset E, Fowler MW, Douglas PL, Entchev E, Douglas MA. Performance comparison of Fick's, dusty-gas and Stefan–Maxwell models to predict the concentration overpotential of a SOFC anode. Journal of Power Sources. 2003;122:9-18.
[23] Chan SH, Khor KA, Xia ZT. A complete polarization model of a solid oxide fuel cell and its sensitivity to the change of cell component thickness. Journal of Power Sources. 2001;93:130-40.
[24] Todd B, Young JB. Thermodynamic and transport properties of gases for use in solid oxide fuel cell modelling. Journal of Power Sources. 2002;110:186-200.
[25] NETL. Fuel Cell Handbook, Seventh Edition. DOE/NETL; 2004. p. CD.
[26] Xu H, Chen B, Zhang H, Tan P, Yang G, Irvine JTS, et al. Experimental and modeling

study of high performance direct carbon solid oxide fuel cell with in situ catalytic steam-carbon gasification reaction. Journal of Power Sources. 2018;382:135-43.
[27] Nam JH, Jeon DH. A comprehensive micro-scale model for transport and reaction in intermediate temperature solid oxide fuel cells. Electrochimica Acta. 2006;51:3446-60.
[28] Jin W, Gu X, Li S, Huang P, Xu N, Shi J. Experimental and simulation study on a catalyst packed tubular dense membrane reactor for partial oxidation of methane to syngas. Chemical Engineering Science. 2000;55:2617-25.
[29] Ni M. 2D heat and mass transfer modeling of methane steam reforming for hydrogen production in a compact reformer. Energy Conversion and Management. 2013;65:155-63.
[30] Ni M. Is steam addition necessary for the landfill gas fueled solid oxide fuel cells? International Journal of Hydrogen Energy. 2013;38:16373-86.

List of Tables

Table 1 Material properties

Parameters	**Value or expression**	**Unit**
Conductivity		
$\boldsymbol{\sigma_{\mathbf{CGO(dense)}}}$	$1.22 \times e^{\frac{16054}{RT}}$ [15]	S m^{-1}
$\boldsymbol{\sigma_{\mathbf{CGO\ (porous)}}}$	$(1-\varepsilon) \times 0.38 \times e^{\frac{16054}{RT}}$ [15]	S m^{-1}
$\boldsymbol{\sigma_{\mathbf{BSCF}}}$	$-24455 + 82.321T - \frac{8.28T^2}{1000} + \frac{2.7778T^3}{10000}$ [15]	S m^{-1}
$\boldsymbol{\sigma_{\mathbf{Ni}}}$	$3.27 \times 10^6 - 1065.3T$ [27]	S m^{-1}
Porosity		
$\boldsymbol{\varepsilon_{\mathbf{an}}}$	0.6 [15]	
$\boldsymbol{\varepsilon_{\mathbf{ca}}}$	0.6 [15]	
$\boldsymbol{\varepsilon_{\mathbf{el}}}$	0.3-0.7	
Anode volume fraction		
$\boldsymbol{V_{\mathbf{CGO}}}$	0.23 [15]	
$\boldsymbol{V_{\mathbf{Ni}}}$	0.77 [15]	
Cathode volume fraction		
$\boldsymbol{V_{\mathbf{CGO}}}$	0.25 [15]	
$\boldsymbol{V_{\mathbf{BSCF}}}$	0.75 [15]	
Triple phase boundary		
$\mathbf{S_{TPB}}$	2.14×10^5 [21]	m^2 m^{-3}

Electrode tortuosity		
$\boldsymbol{\tau_{an}}$	3	
$\boldsymbol{\tau_{ca}}$	3	

Table 2 Chemical reaction parameters

Reaction	**Unit**
Methane oxidization reaction rate	
$5 \times 10^4 \times e^{\frac{-166000}{RT}} \times p_{CH_4} \times p_{O_2}$ (anode) [28]	mol m^3 s^{-1}
$1.1 \times e^{\frac{-166000}{RT}} \times p_{CH_4} \times p_{O_2}$ (other area) [28]	mol m^3 s^{-1}
Hydrogen oxidization reaction rate	
$5 \times 10^4 \times e^{\frac{-48484}{RT}} \times p_{CH_4} \times p_{O_2}^{0.5}$ [28]	mol m^3 s^{-1}
Carbon monoxide oxidization reaction rate	
$5 \times 10^4 \times e^{\frac{-47773}{RT}} \times p_{CO} \times p_{O_2}^{0.5}$ [28]	mol m^3 s^{-1}
Methane steam reforming reaction rate	
$2.395 \times 10^7 \times e^{\frac{-231266}{RT}} \times (p_{CH_4} \times p_{H_2O} - \frac{p_{CH_4}^3 \times p_{CO}}{K_{pr}})$ [29]	mol m^3 s^{-1}
$K_{pr} = 1.0267 \times 10^{10} \times e^{-0.2513 \times Z^4 + 0.3665 \times Z^3 + 0.5810 \times Z^2 - 27.134 \times Z + 3.277}$	
$Z = \frac{T}{1000}$	
Water gas shift reaction rate	
$0.0171 \times e^{\frac{-103191}{RT}} \times (p_{CO} \times p_{H_2O} - \frac{p_{H_2} \times p_{CO_2}}{k_{ps}})$ [30]	mol m^3 s^{-1}
$k_{ps} = e^{-0.2935 \times Z^3 + 0.6351 \times Z^2 + 4.1788 \times Z + 0.0169}$	
$Z = \frac{T}{1000}$	

Table 3 Electrochemical reaction parameters [17]

Parameter	**Value**	**Unit**
γ_{H_2}	3.68×10^9	A m^{-2}
E_{act,H_2}	1.2×10^5	J mol^{-1}
γ_{O_2}	1.39×10^{10}	A m^{-2}
E_{act,O_2}	1.2×10^5	J mol^{-1}
γ_{CO}	1.67×10^9	A m^{-2}
$E_{act,CO}$	1.2×10^5	J mol^{-1}
α_{H_2}	0.5	
α_{CO}	0.5	
α_{O_2}	0.5	

List of Figures

Fig.1 (a)Schematic of a button all-porous solid oxide fuel cell; (b) Schematic of a tubular all-porous solid oxide fuel cell; (c)Model validation for the button all-porous solid oxide fuel cell; (d)Electrochemical performance comparison between button and tubular all-porous solid oxide fuel cells.

Fig. 2 (a) The current density and anode surface O/C ratio change with different electrolyte porosities at 923 K operating temperature, 0.5 V operating voltage, 100 SCCM inlet gas flow rate, 35 % methane for anode inlet and air for cathode inlet; (b) $CH_4 \times O_2$ mole fraction product distribution in 0.3 and 0.7 electrolyte porosity cases; (c) Molar fraction distribution of H_2 and CO in 0.3 and 0.7 electrolyte porosity cases.

Fig. 3 (a) The current density change with different inlet CH_4 mole fraction at 923 K operating temperature, 0.5 V operating voltage, 100 SCCM inlet gas flow rate and air for cathode inlet in 0.3, 0.5 and 0.7 electrolyte porosity cases; (b) Outlet H_2, CO and CH_4 mole fraction change with different inlet CH_4 mole fraction in 0.3, 0.5 and 0.7 electrolyte porosity cases; (c) Anode surface average O/C ratio change with different inlet CH_4 mole fraction in 0.3, 0.5 and 0.7 electrolyte porosity cases; (d) Peak value of $CH_4 \times O_2$ mole fraction product change with different inlet CH_4 mole fraction in 0.3, 0.5 and 0.7 electrolyte porosity cases;

Fig. 4 (a) The current density change with different inlet gas flow rate at 923 K operating temperature, 0.5 V operating voltage, pure methane for anode inlet and pure oxygen for cathode inlet in 0.3, 0.5 and 0.7 electrolyte porosity cases; (b) Outlet H_2, CO and CH_4 mole fraction

change with different inlet gas flow rate at 0.5 electrolyte porosity; (c) Anode surface average O/C ratio change with different inlet gas flow rate in 0.3, 0.5 and 0.7 electrolyte porosity cases; (d) Anode surface O/C ratio change along the cell length contributed by H_2O and O_2 at 50 SCCM and 0.3 electrolyte porosity.

Fig. 5 (a) The I-V-P characteristics comparison between experimental all porous solid oxide fuel cell (old) and design solid oxide fuel cell with partial porous electrolyte (new) at 923 K operating temperature, 0.3 methane mole fraction for anode inlet and air for cathode inlet; (b) Anode surface O/C ratio change at different applied voltages in the new design; (c) Peak value of $CH_4 \times O_2$ mole fraction product change at different applied voltages in the new design; (d) Outlet H_2, CO and CH_4 mole fraction change at different applied voltages in the new design;

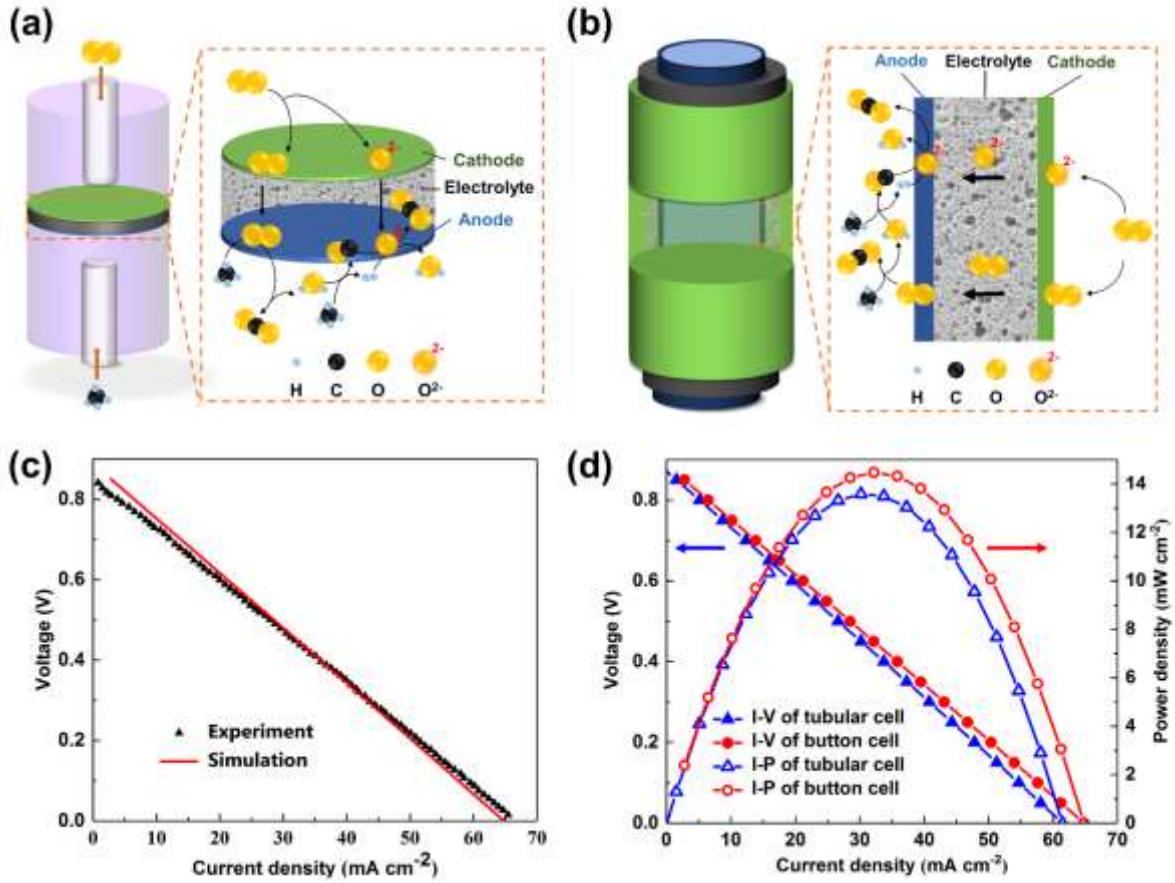

Fig.1 (a)Schematic of a button all-porous solid oxide fuel cell; (b) Schematic of a tubular all-porous solid oxide fuel cell; (c)Model validation for the button all-porous solid oxide fuel cell; (d)Electrochemical performance comparison between button and tubular all-porous solid oxide fuel cells.

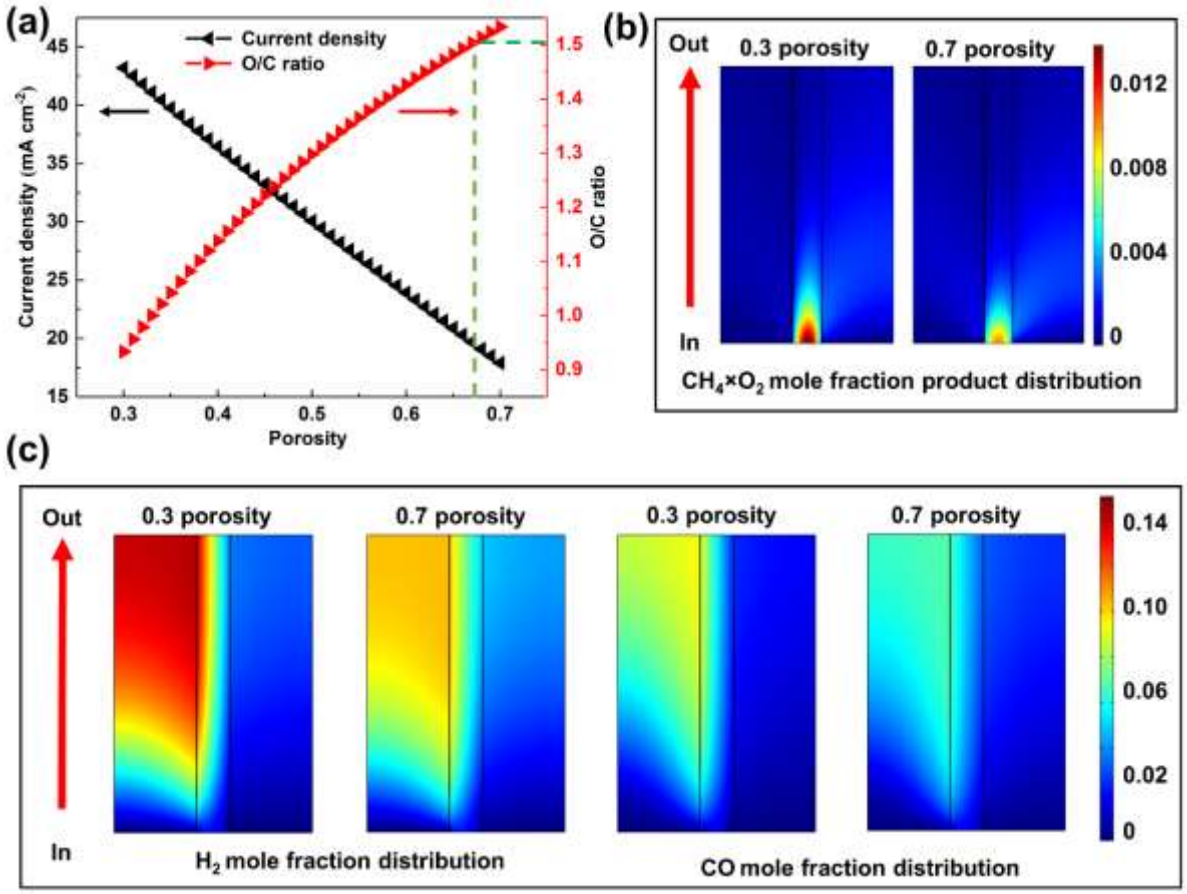

Fig. 2 (a) The current density and anode surface O/C ratio change with different electrolyte porosities at 923 K operating temperature, 0.5 V operating voltage, 100 SCCM inlet gas flow rate, 35 % methane for anode inlet and air for cathode inlet; (b) $CH_4 \times O_2$ mole fraction product distribution in 0.3 and 0.7 electrolyte porosity cases; (c) Molar fraction distribution of H_2 and CO in 0.3 and 0.7 electrolyte porosity cases.

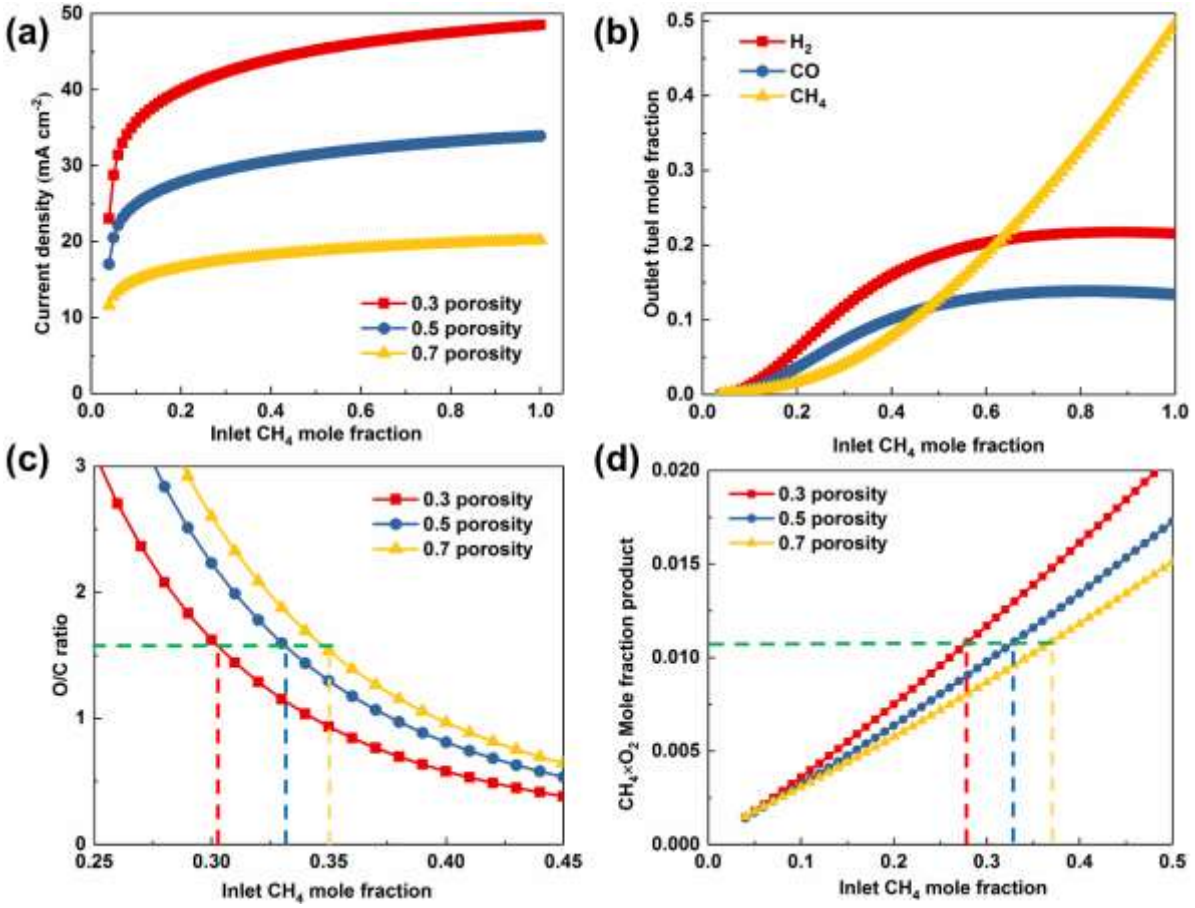

Fig. 3 (a) The current density change with different inlet CH_4 mole fraction at 923 K operating temperature, 0.5 V operating voltage, 100 SCCM inlet gas flow rate and air for cathode inlet in 0.3, 0.5 and 0.7 electrolyte porosity cases; (b) Outlet H_2, CO and CH_4 mole fraction change with different inlet CH_4 mole fraction in 0.3, 0.5 and 0.7 electrolyte porosity cases; (c) Anode surface average O/C ratio change with different inlet CH_4 mole fraction in 0.3, 0.5 and 0.7 electrolyte porosity cases; (d) Peak value of CH_4×O_2 mole fraction product change with different inlet CH_4 mole fraction in 0.3, 0.5 and 0.7 electrolyte porosity cases;

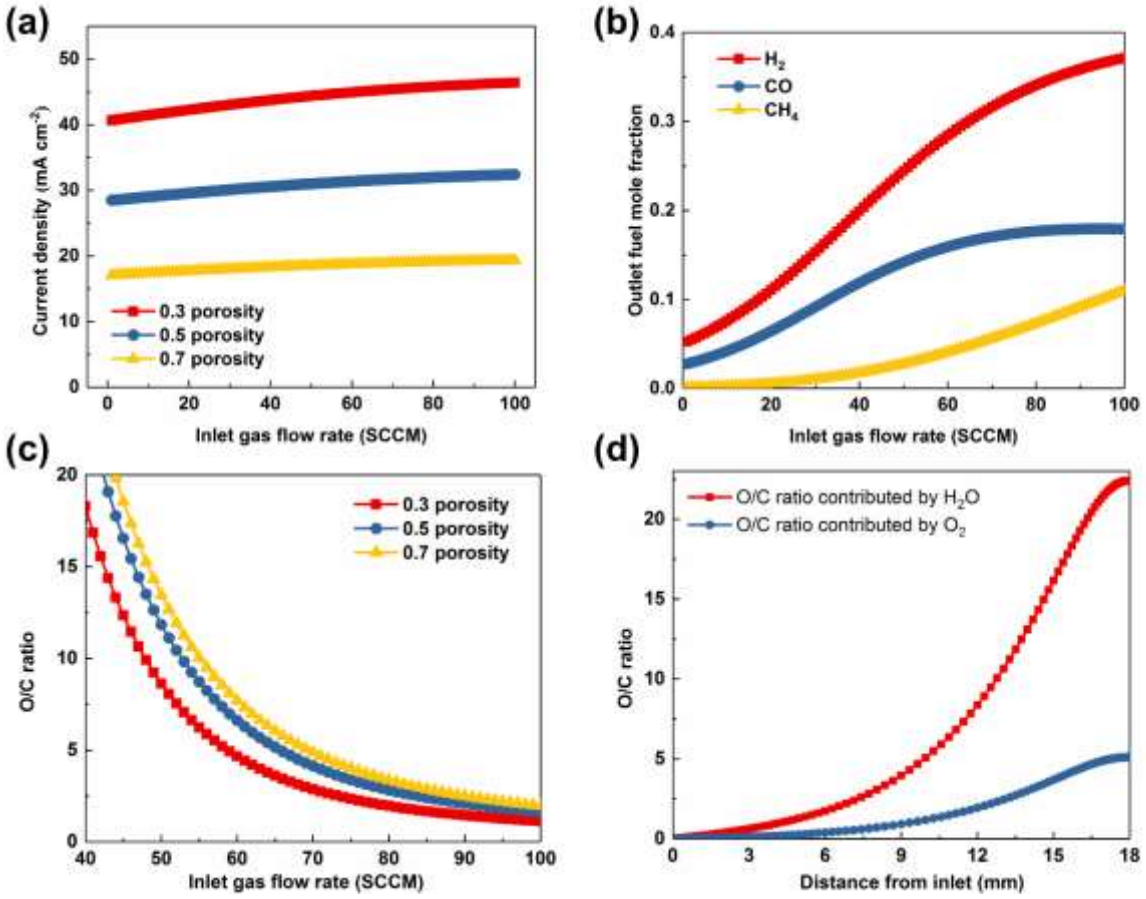

Fig. 4 (a) The current density change with different inlet gas flow rate at 923 K operating temperature, 0.5 V operating voltage, pure methane for anode inlet and pure oxygen for cathode inlet in 0.3, 0.5 and 0.7 electrolyte porosity cases; (b) Outlet H_2, CO and CH_4 mole fraction change with different inlet gas flow rate at 0.5 electrolyte porosity; (c) Anode surface average O/C ratio change with different inlet gas flow rate in 0.3, 0.5 and 0.7 electrolyte porosity cases; (d) Anode surface O/C ratio change along the cell length contributed by H_2O and O_2 at 50 SCCM and 0.3 electrolyte porosity.

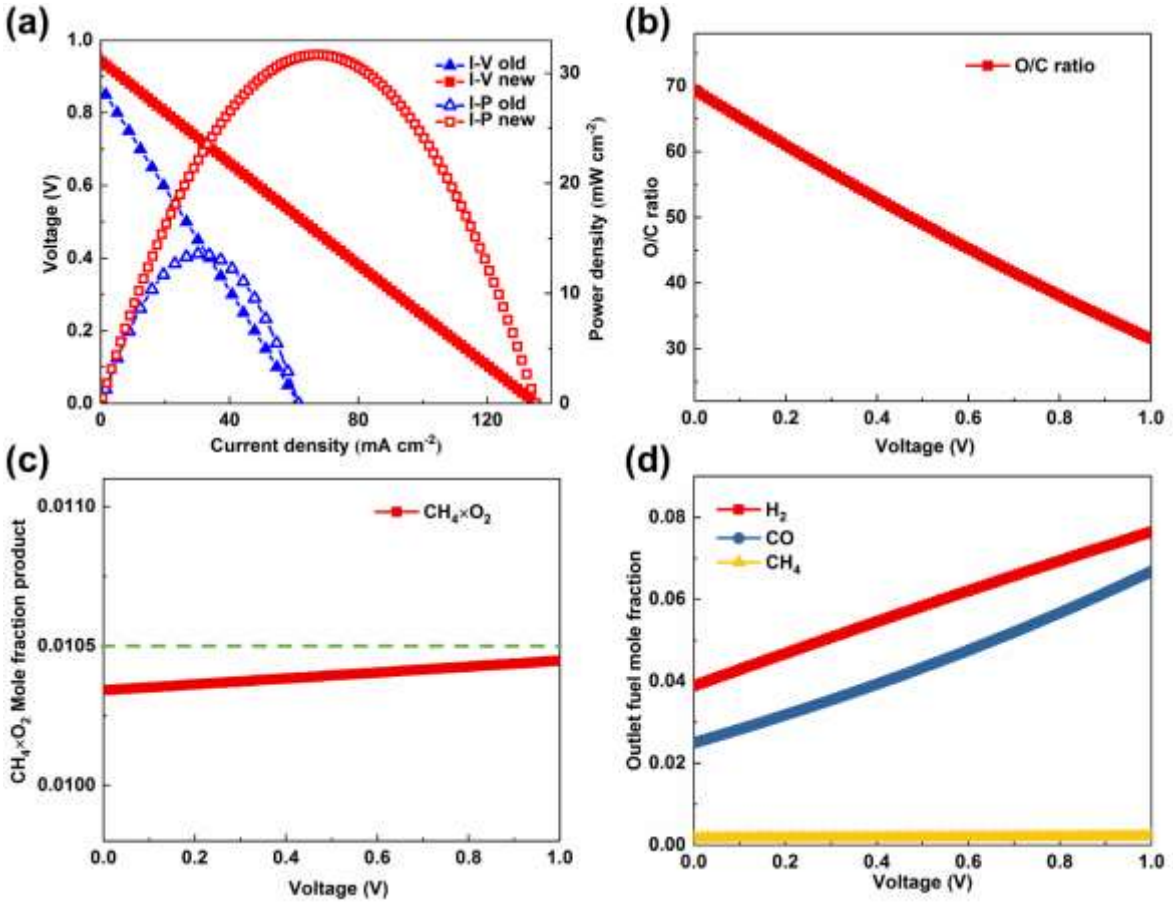

Fig. 5 (a) The I-V-P characteristics comparison between experimental all porous solid oxide fuel cell (old) and design solid oxide fuel cell with partial porous electrolyte (new) at 923 K operating temperature, 0.3 methane mole fraction for anode inlet and air for cathode inlet; (b) Anode surface O/C ratio change at different applied voltages in the new design; (c) Peak value of $CH_4 \times O_2$ mole fraction product change at different applied voltages in the new design; (d) Outlet H_2, CO and CH_4 mole fraction change at different applied voltages in the new design;